IJMMM International Journal of Minerals, Metallurgy and Materials 矿物冶金与材料学报（英文版）

Mineral transition and formation mechanism of calcium aluminate compounds in $CaO-Al_2O_3-Na_2O$ system during high-temperature sintering

Hai-yan Yu, Xiao-lin Pan, Yong-pan Tian, and Gan-feng Tu

Cite this article as:
Hai-yan Yu, Xiao-lin Pan, Yong-pan Tian, and Gan-feng Tu, Mineral transition and formation mechanism of calcium aluminate compounds in $CaO-Al_2O_3-Na_2O$ system during high-temperature sintering, *Int. J. Miner. Metall. Mater.*, 27(2020), No. 7, pp. 924-932. https://doi.org/10.1007/s12613-019-1951-1

International Journal of Minerals, Metallurgy and Materials
Volume 27, Number 7, July 2020, Page 924
https://doi.org/10.1007/s12613-019-1951-1

Mineral transition and formation mechanism of calcium aluminate compounds in $CaO-Al_2O_3-Na_2O$ system during high-temperature sintering

Hai-yan Yu, Xiao-lin Pan, Yong-pan Tian, and Gan-feng Tu

School of Metallurgy, Northeastern University, Shenyang 110819, China
(Received: 4 September 2019; revised: 21 November 2019; accepted: 25 November 2019)

Abstract: The mineral transition and formation mechanism of calcium aluminate compounds in $CaO-Al_2O_3-Na_2O$ system during the high-temperature sintering process were systematically investigated using DSC−TG, XRD, SEM−EDS, FTIR, and Raman spectra, and the crystal structure of $Na_4Ca_3(AlO_2)_{10}$ was also simulated by Material Studio software. The results indicated that the minerals formed during the sintering process included $Na_4Ca_3(AlO_2)_{10}$, $CaO{\cdot}Al_2O_3$, and $12CaO{\cdot}7Al_2O_3$, and the content of $Na_4Ca_3(AlO_2)_{10}$ could reach 92wt% when sintered at 1200°C for 30 min. The main formation stage of $Na_4Ca_3(AlO_2)_{10}$ occurred at temperatures from 970 to 1100°C, and the content could reach 82wt% when the reaction temperature increased to 1100°C. The crystal system of $Na_4Ca_3(AlO_2)_{10}$ was tetragonal, and the cells preferred to grow along crystal planes (110) and (210). The formation of $Na_4Ca_3(AlO_2)_{10}$ was an exothermic reaction that followed a secondary reaction model, and its activation energy was 223.97 kJ/mol.

Keywords: calcium aluminate; sodium oxide; crystal structure; formation kinetics; sintering

1. Introduction

The formation theories and applications of calcium aluminates within the $CaO-Al_2O_3-SiO_2$ ternary system have been the focus of research for centuries and play important roles in oxide ceramics, cement chemistry, metallurgical slags, refractories, biomaterials, and geochemistry [1−4]. These calcium aluminate compounds mainly comprise $CaAl_{12}O_{19}$ (CA_6), $CaAl_4O_7$ (CA_2), $CaAl_2O_4$ (CA), $Ca_{12}Al_{14}O_{33}$ ($C_{12}A_7$), and $Ca_3Al_2O_6$ (C_3A) [5−6]. Na_2O has been reported not only to form a solid solution in calcium aluminates during a high-temperature solid-state reaction, but also to form a variety of compounds such as $Na_2CaAl_4O_8$ ($Na_2O{\cdot}CaO{\cdot}2Al_2O_3$, NCA_2), $Na_4Ca_3Al_{10}O_{20}$ ($2Na_2O{\cdot}3CaO{\cdot}5Al_2O_3$, $N_2C_3A_5$), and $Na_2Ca_3Al_{16}O_{28}$ ($Na_2O{\cdot}3CaO{\cdot}8Al_2O_3$, NC_3A_8) according to the ternary phase diagram of the $Na_2O-CaO-Al_2O_3$ system [7−9].

Shen *et al*. [10] found that the structure of $C_{12}A_7$ does not change when doped with a small amount of Na_2O, but its antibacterial activities are improved. Ostrowski and Żelazny [11] found that when the Na_2O content in CA is less than 10wt%, CA will gradually convert to $C_{12}A_7$ and $N_2C_3A_5$, and as the Na_2O content increases to 15wt%, a C_3A-Na_2O solid solution forms and the amounts of $C_{12}A_7$ and $N_2C_3A_5$ decrease. When the Na_2O content is increased to 25wt%, the amount of C_3A-Na_2O solid solution decreases, whereas the amounts of $Na_2O{\cdot}Al_2O_3$ (NA) and free calcium oxide increase. The results of our previous study [12] indicated that Na_2O can form a solid solution in $C_{12}A_7$, increase the volume of the elementary cell of $C_{12}A_7$, and decrease its formation temperature. $N_2C_3A_5$ can also form when the Na_2O content is less than 4.26wt%, and both possess good alumina leaching ability in alkali solution. The eutectic reactions of $C_{12}A_7$, CA, and $N_2C_3A_5$ have been reported to occur at a composition of 38wt% CaO, 4wt% Na_2O, and 58wt% Al_2O_3, and $N_2C_3A_5$ can transform into $C_{12}A_7$ by the loss of Na_2O [7].

Based on the above results, a low content of Na_2O can form C_3A-Na_2O and $C_{12}A_7-Na_2O$ solid solutions in a $CaO-Al_2O_3-Na_2O$ system when sintered at elevated temperatures, and transform into $N_2C_3A_5$ and NA, respectively, as the Na_2O content increases. However, the formation process and mechanism of $N_2C_3A_5$ are as yet unclear, and most research on $N_2C_3A_5$ has involved the indirect reactions between calcium aluminate compounds and Na_2O. In this work, first, we used Material Studio software to predict the crystal structure of $N_2C_3A_5$ and then systematically studied the mineral transformation and formation kinetics of $N_2C_3A_5$ during the heating and sintering processes by differential scanning

Corresponding author: Xiao-lin Pan E-mail: panxl@smm.neu.edu.cn

calorimetry−thermogravimetry (DSC−TG), X-ray diffraction (XRD), scanning electron spectroscopy−energy dispersive X-ray spectroscopy (SEM−EDS), Fourier-transform infrared spectroscopy (FTIR), and Raman spectroscopy.

2. Experimental

2.1. Materials

Analytically pure reagents of $CaCO_3$, Al_2O_3, and Na_2CO_3 were used in this study. The molar ratio of $CaCO_3$ to Al_2O_3 was 0.60 and that of Na_2CO_3 to Al_2O_3 was 0.40, according to the stoichiometry of $N_2C_3A_5$. Prior to sintering, the raw materials were mixed for 3 h by ZrO_2 balls.

2.2. Equipment and methods

The mixtures were sintered in a $MoSi_2$ resistance furnace (KSL-1700X-A2). The XRD data were obtained using a Philips PW3040/60 with Cu K_α radiation operated at 40 kV and 40 mA, and these data were analyzed using MDI Jade software with the PDF2−2004 database. To index the XRD patterns, the TREOR program Reflex in the Material Studio software was used. The microstructures of the sintered samples were analyzed using SEM (SHIMADZU SSX-550) and EDS (DX-4). The differential thermal analyzer (DSC, SDT-Q600-V8.0-Build 95) was used to determine the mass and heat changes during the heating process with a heating rate of 10°C/min. Fourier transform infrared spectroscopy (FTIR, SHIMADZU IR Prestige-21) was used to study the absorption spectra of sintered samples with the matrix material of KBr, for which the scanning range is 400−4000 cm^{-1} and the instrument resolution is 4 cm^{-1}. The Raman spectrum characteristics of the sintered samples were analyzed by a laser focused Raman analyzer (HR800), using a test wavelength of 488 nm and a laser power of 0.8 W.

3. Results and discussion

3.1. Crystal structure of $N_2C_3A_5$

Authors have found that with different molar ratios of CaO to Al_2O_3, C_3A, $C_{12}A_7$, CA, CA_2, and CA_6 can form during the sintering process when the temperature ranges from 1100 to 1400°C. These various calcium aluminates play a major role as intermediate phases prior to the final equilibrium phases [13−14]. However, the stoichiometry, crystal structure, and formation mechanism of $N_2C_3A_5$ as the target phase by direct reaction are unknown. The mixed materials of $CaCO_3$, Al_2O_3, and Na_2CO_3 were sintered at 1100, 1150, 1200, and 1250°C for 30 min, and the resulting XRD patterns are shown in Fig. 1. The products were mainly $N_2C_3A_5$, although small amounts of CA and $C_{12}A_7$ were still present. We chose the XRD pattern of the product sintered at 1200°C for the crystal indexing of $N_2C_3A_5$, because its $C_{12}A_7$ peak intensities are the weakest of all the XRD patterns. The $N_2C_3A_5$ content in the product was calculated to be about 92wt%.

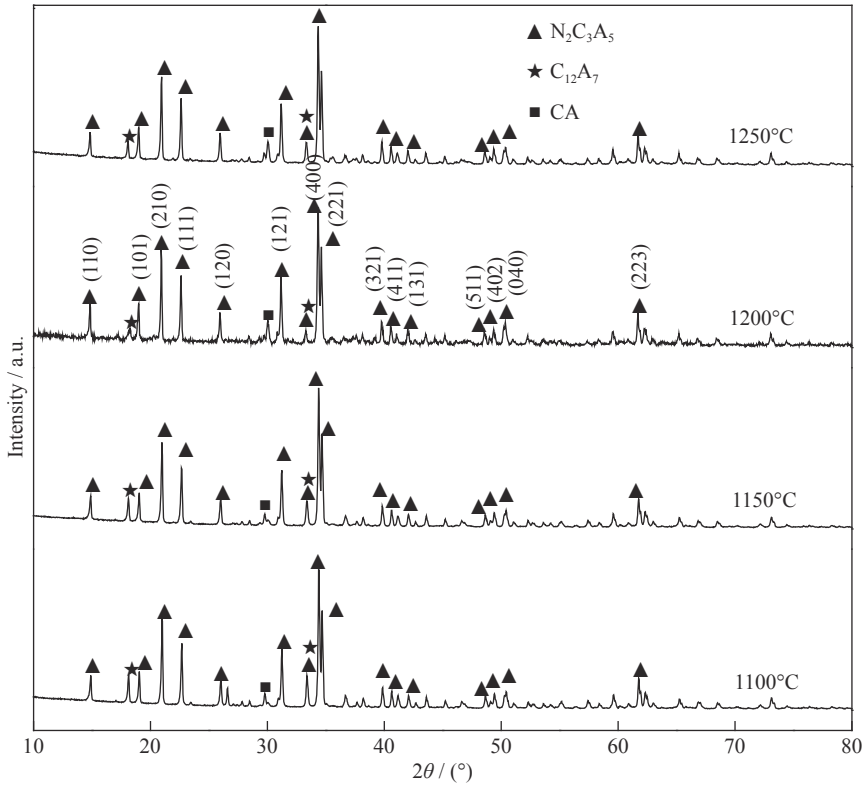

Fig. 1. XRD patterns of products sintered at 1100−1250°C for 30 min.

Fig. 1 shows the crystal planes corresponding to the characteristic peaks of $N_2C_3A_5$. The characteristic peak of crystallographic plane (400) is the highest. As shown in Table 1, the lattice constants of a and b are 1.0457 nm and 0.7265 nm, respectively, which are similar to the results (a = 1.0435 nm, b = 0.7254 nm) reported by Verweij and Saris [7].

Table 1. Lattice constants and crystal structure parameters of $N_2C_3A_5$

Crystal system	Space group	a / nm	b / nm	c / nm	$\alpha = \beta = \gamma$ / (°)	Volume / nm^3
Tetragonal	P222	1.0457	0.7265	0.5215	90	0.3962

According to references [15−16], the vibrational peaks of the Raman spectrum of $C_{12}A_7$ are as follows: the bands at 521 and 779 cm^{-1} represent the vibrations of the Al−O skeleton and the binding O^{2-} in the cage, respectively; the bands at 834 and 912 cm^{-1} represent the vibration of the Al−O skeleton; and the bands at 338 and 887 cm^{-1} represent the vibration of O^{2-} on the skeleton. According to reference [17], the vibrational peaks of the Raman spectrum of CA are as follows: the weak band at 558 cm^{-1} represents the vibration of the O atom in the Al−O−Al connecting structure; the vibrational peaks at 785 and 895 cm^{-1} represent the stretching vibrations of the Al−O bond. Fig. 2 shows the Raman spectrum of the product sintered at 1200°C for 30 min. Based on the characteristic absorption peaks of $C_{12}A_7$ and CA, the Raman characteristic absorption peaks of $N_2C_3A_5$ are 524, 789, 1590, and 2712 cm^{-1}. The bands at 524 and 785 cm^{-1} represent the vibrations of the Al−O bond on the skeleton of the $N_2C_3A_5$ structure.

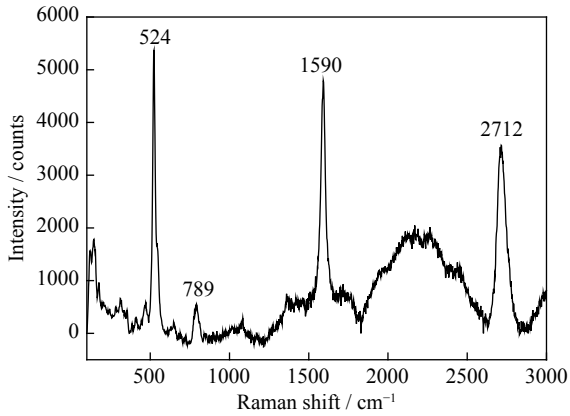

Fig. 2. Raman spectrum of product sintered at 1200°C for 30 min.

3.2. Formation characteristics of $N_2C_3A_5$

Fig. 3 shows the DSC−TG results of the Na_2CO_3−$CaCO_3$−Al_2O_3 mixture. The mass losses of CO_2 decomposed by $CaCO_3$ and Na_2CO_3 were calculated to be 12.9wt% and 8.6wt%, respectively. The mass loss between points A and B was about 11.5wt%, and that between B and D was about 9wt%. It can be concluded that $CaCO_3$ decomposed first at a temperature within the range between A and B. The reaction temperatures of Na_2CO_3 were between B and D. Considering that the decomposition of $CaCO_3$ is an endothermic reaction, the only exothermic peak that occurs above 900°C on the DSC−TG curves indicates the formation reaction of $N_2C_3A_5$.

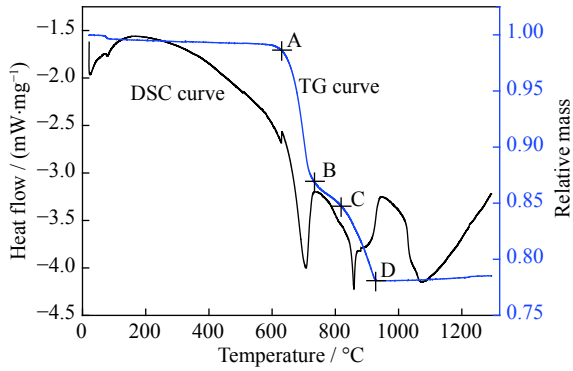

Fig. 3. DSC−TG results of Na_2CO_3−$CaCO_3$−Al_2O_3 mixture.

Next, the formation characteristics of $N_2C_3A_5$ were studied during the heating process when the temperature increased from room temperature to 1300°C with no duration. The sintered products were produced by air cooling at temperatures of 630, 700, 800, 860, 930, 970, 1000, 1040, 1100, 1200, and 1300°C, respectively. These products were then mixed with 10wt% MgO, and their corresponding XRD patterns are shown in Figs. 4−6. When the temperature was below 860°C, the reactions mainly comprised the decomposition of $CaCO_3$. The content of $C_{12}A_7$ increased when the sintering temperature increased from 800 to 970°C, and a small amount of CA also formed. However, the content of $C_{12}A_7$ decreased when the temperature was higher than 1000°C, and it almost disappeared at 1100°C.

The crystal planes (110) and (210) of $N_2C_3A_5$ first formed when the temperature reached 800°C. As the temperature increased to 970°C, the characteristic peak of crystal plane (400) became highest, and was the same as the XRD patterns of stable $N_2C_3A_5$. The contents of CaO and Al_2O_3 obviously decreased when the temperature increased from 1040 to 1100°C. Therefore, the formation process of $N_2C_3A_5$ can be divided into three stages: the main formation stage of the $N_2C_3A_5$ crystal structure occurring between 860 and 1000°C, the second stage involving the transformation from $C_{12}A_7$ to $N_2C_3A_5$ between 1000 and 1040°C, and the final phase transformation of the diffusion of the remaining CaO and Al_2O_3 into the crystal structure of $N_2C_3A_5$. The sintering reactions were absolutely complete when the temperature reached 1200°C.

The crystallinity indicates the relative proportions of the amorphous and crystalline phases when amorphous peaks occur in the XRD patterns; otherwise, this term is determ-

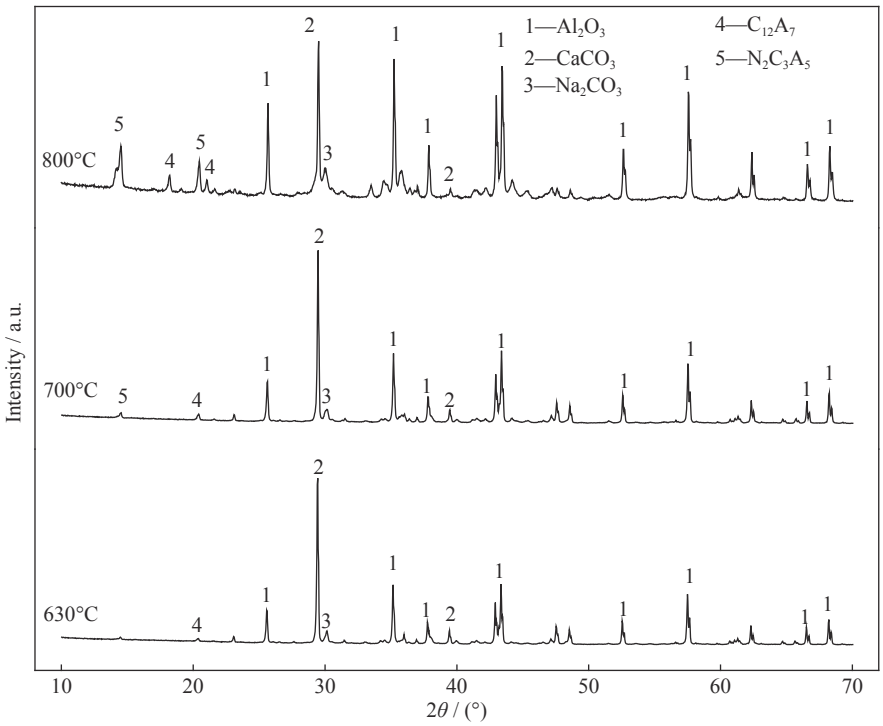

Fig. 4. XRD patterns of products sintered at 630−800°C.

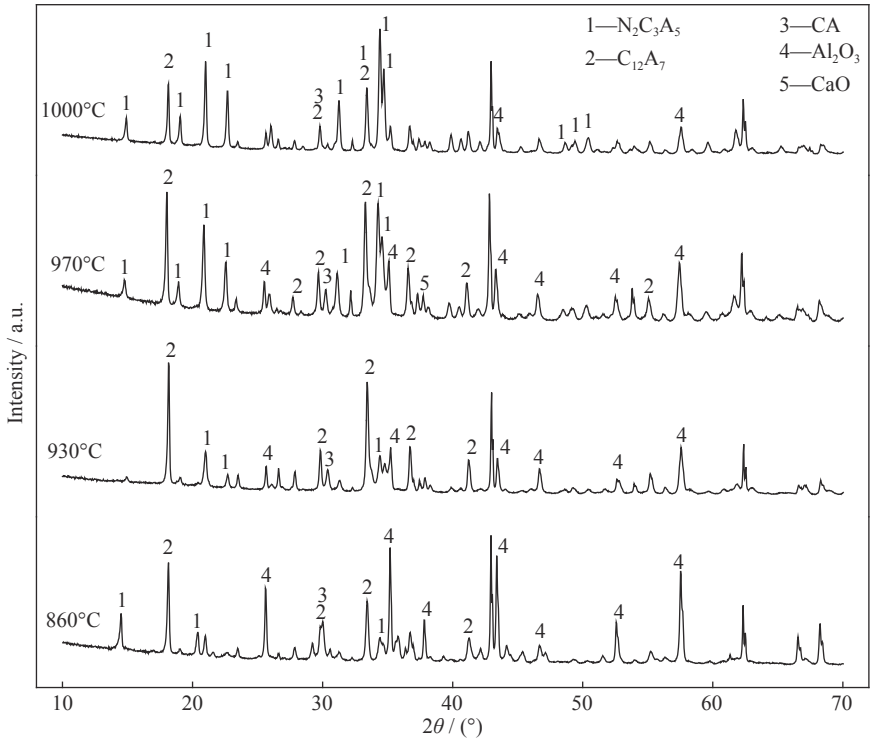

Fig. 5. XRD patterns of products sintered at 860−1000°C.

ined by the degree of crystallization of the crystalline phases. There were no amorphous peaks in the XRD spectra of products sintered at 630−1300°C; therefore, the crystallinity of $N_2C_3A_5$ was indicated by its degree of crystallization. Figs. 7 and 8 show the calculated full width at half maximum (FWHM) of the XRD spectra and the crystallinity of $N_2C_3A_5$ with different crystal planes, respectively. In Fig. 7, the FWHM decreased with increasing temperature, which suggested that the $N_2C_3A_5$ crystals grew along the (400) and (210) planes. The crystallinity also decreased with the crystal

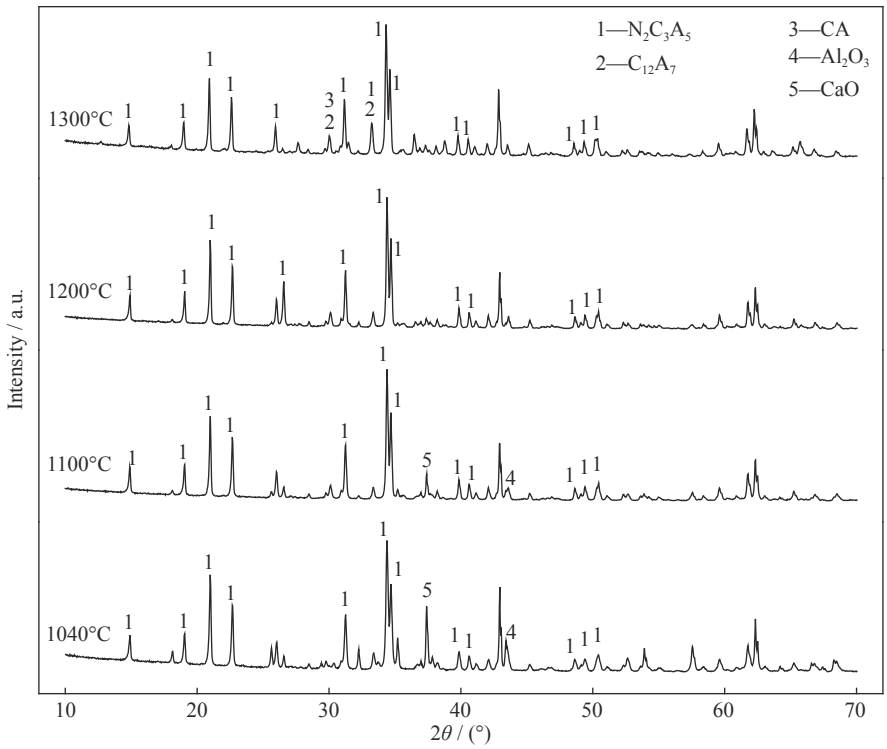

Fig. 6. XRD patterns of products sintered at 1040−1300°C.

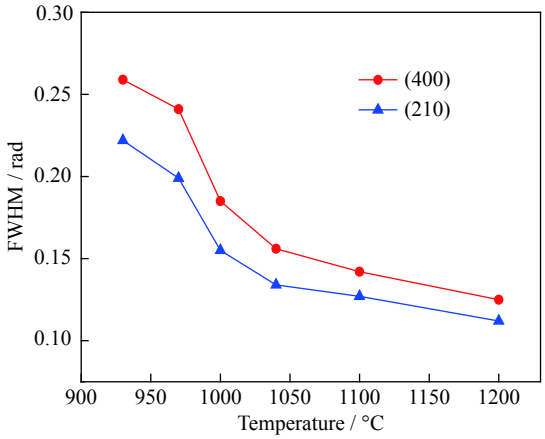

Fig. 7. FWHM of $N_2C_3A_5$ with different crystal planes sintered at different temperatures.

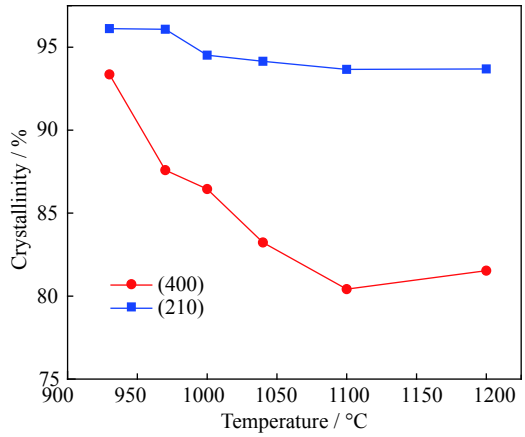

Fig. 8. Crystallinity of $N_2C_3A_5$ with different crystal planes sintered at different temperatures.

growth. The crystallinity of $N_2C_3A_5$ in the crystal plane (210) was greater than that of (400), since crystal plane (210) formed first. Meanwhile, the remaining CaO and Al_2O_3 reacted completely at the above temperature ranges. Therefore, the increasing crystallinity was due to the diffusion of CaO and Al_2O_3 into the $N_2C_3A_5$ crystal.

Figs. 9−11 show the FTIR spectra of the mixture of Al_2O_3, Na_2CO_3, and $CaCO_3$ when heated from 630 to 1300°C. According to references [18−20], the absorption bands at 876 and 712 cm^{-1} indicate the in-plane and out-plane vibrations of CO_3^{2-}, respectively, and the absorption bands at 637, 592, 490, and 451 cm^{-1} can be attributed to the characteristic peaks of α-Al_2O_3. As the heating temperature increases, the band at 876 cm^{-1} was replaced by those at 870 and 885 cm^{-1} because of the decomposition of $CaCO_3$. The bands at 870, 885, and 712 cm^{-1} disappeared when the temperature increased to 930°C, which indicated that the Na_2CO_3 reaction was complete. The reactions of Al_2O_3, Na_2CO_3, and $CaCO_3$ broadened the absorption bands at 592 and 451 cm^{-1}. When the reaction temperature reached 930°C, the band at 637 cm^{-1} disappeared, and the bands at 592 and 490 cm^{-1} were replaced by those at 571 and 455 cm^{-1}. The broadening of 571 and 459 cm^{-1} in samples heated to 930, 970, and 1000°C, and the existence of a wide absorption band centered

at 830 cm^{-1} indicated that the crystal structures of products had a short-range order. According to the XRD results, the absorption bands of $N_2C_3A_5$ were located at 704 and 772 cm^{-1}, with the former attributable to the Al−O stretching vibration of the AlO_6 octahedron. According to the FTIR results in this work, the formation temperatures of the $N_2C_3A_5$ structure were mainly between 970 and 1040°C, which was consistent with the XRD results; the absorption bands of products reacting at temperatures higher than 1100°C did not change, which was mainly attributed to the diffusion of CaO in $N_2C_3A_5$, and then improved the crystal structure of $N_2C_3A_5$.

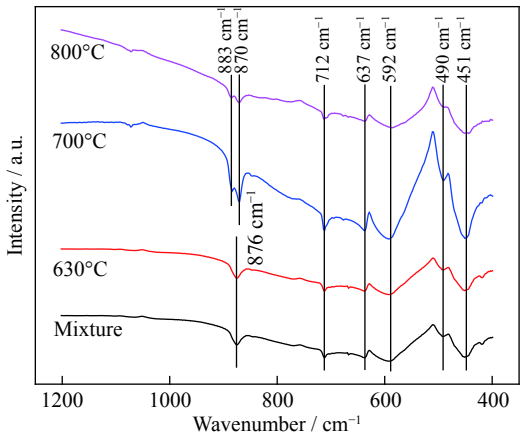

Fig. 9. FTIR spectra of the mixture of raw materials and products sintered at 630−800°C.

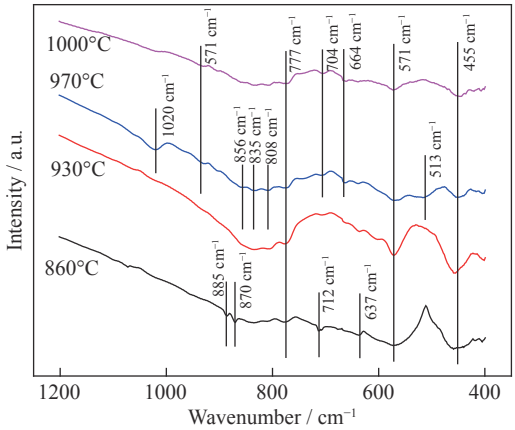

Fig. 10. FTIR spectra of products sintered at 860−1000°C.

3.3. Morphology of $N_2C_3A_5$

To study the morphology of $N_2C_3A_5$, the product sintered at 1200°C for 30 min was used as shown in Fig. 12. The particles can be clearly categorized as either bulk or powder. As shown in Figs. 13(a)−13(d), the bulk particles had higher Na and Al contents, whereas the powder particles had a higher Ca content.

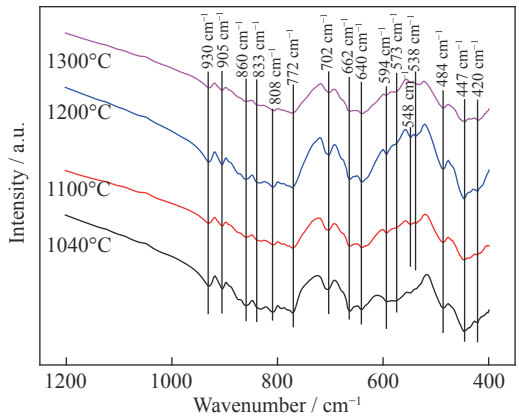

Fig. 11. FTIR spectra of products sintered at 1040−1300°C.

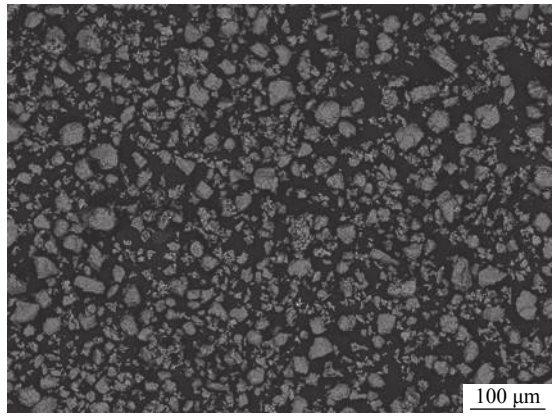

Fig. 12. Macrostructure of the product sintered at 1200°C for 30 min.

Table 2 shows the EDS results of the elemental analyses, the calculated $M_{CaO}/M_{Al_2O_3}$ ratios (molar ratio of CaO to Al_2O_3), and the $M_{Na_2O}/M_{Al_2O_3}$ ratios (molar ratio of Na_2O to Al_2O_3). The $M_{CaO}/M_{Al_2O_3}$ and $M_{Na_2O}/M_{Al_2O_3}$ ratios of points A and B in Fig. 13(a) (corresponding magnified images are shown in Figs. 13(e) and 13(f), respectively) were similar to those for $N_2C_3A_5$, so the bigger particles were $N_2C_3A_5$. The formula for this compound can be expressed as $xNa_2O{\cdot}yCaO{\cdot}zAl_2O_3$ (x/z = 0.4−0.5, y/z = 0.5−0.6). The diameter of $N_2C_3A_5$ was about 30 μm. The $M_{CaO}/M_{Al_2O_3}$ ratio of the small particles (point C in Fig. 13(a)) was about 1.21, which may represent a region wherein CA, $C_{12}A_7$, and $N_2C_3A_5$ coexist.

3.4. Formation kinetics of $N_2C_3A_5$

The products sintered to 970, 1000, 1040, 1100°C were used to analyze the formation kinetics of $N_2C_3A_5$. The phase contents in the sintered products can be calculated by the intensity of the peaks (I) and the reference intensity ratios (RIRs) of the phases. As the RIR value of $N_2C_3A_5$ has not been published, we calculated the $N_2C_3A_5$ content using the internal standard method. The products after heating to different

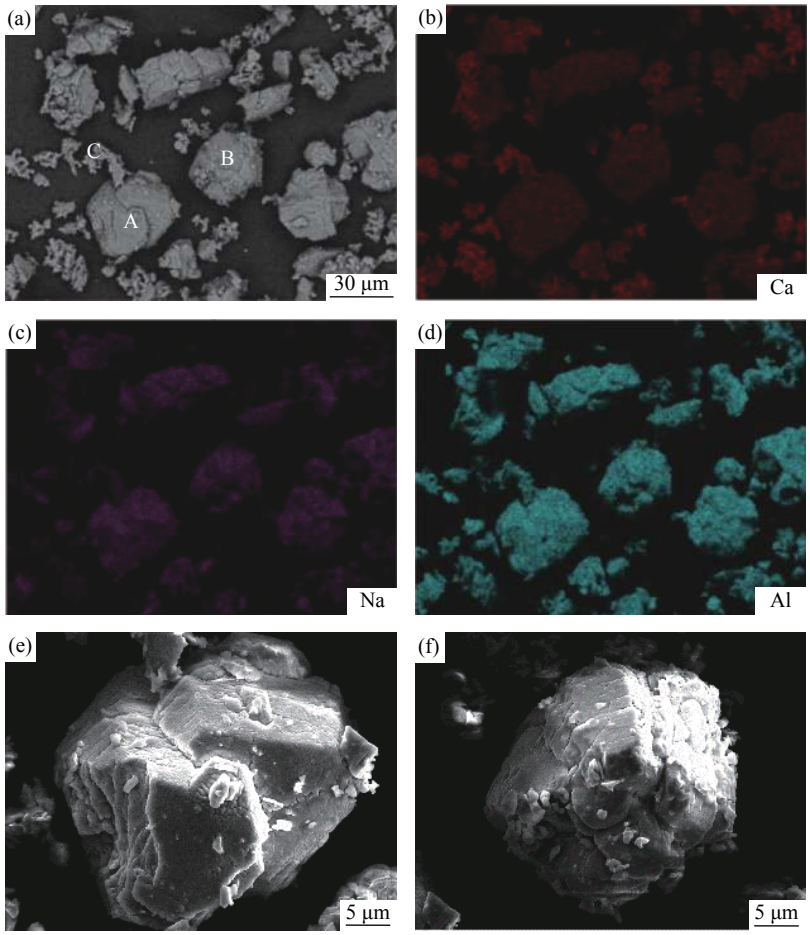

Fig. 13. SEM results of the product sintered at 1200°C for 30 min: (a) backscattered electron image; (b–d) scanning maps corresponding to (a); (e, f) magnification of A and B in (a).

Table 2. EDS results of the points in Fig. 13(a)

Point	O / mol%	Al / mol%	Ca / mol%	Na / mol%	$M_{Na_2O}/M_{Al_2O_3}$	$M_{CaO}/M_{Al_2O_3}$
A	50.89	28.60	7.38	13.13	0.46	0.52
B	51.13	28.61	7.63	12.63	0.44	0.53
C	61.94	21.54	13.05	3.47	0.16	1.21

temperatures were mixed with MgO and α-Al_2O_3 as follows: an MgO content of 10wt%, sintered product contents of 5wt%, 10wt%, 30wt%, 60wt%, and 80wt% respectively, and the rest of α-Al_2O_3. The content of $N_2C_3A_5$ in the sintered products was calculated using the union of Eqs. (1) and (2). Fig. 14 shows the linear relationship between $\omega_{N_2C_3A_5}$ and $I_{N_2C_3A_5}/I_{MgO}$, for which the linear correlation coefficient (R^2) value is 0.9981. The $N_2C_3A_5$ content in the sintered products increased as the reaction temperature increased.

$$\omega_\alpha = \frac{I_\alpha/\mathrm{RIR}_\alpha}{\sum_i (I_i/\mathrm{RIR}_i)} \times 100\% \quad (1)$$

$$I_{N_2C_3A_5}/I_{MgO} = \frac{\mathrm{RIR}_{N_2C_3A_5}}{\mathrm{RIR}_{MgO} \times \omega_{MgO}} \times \omega_{N_2C_3A_5} \quad (2)$$

where ω_α, ω_{MgO}, and $\omega_{N_2C_3A_5}$ are the mass fractions of α-Al_2O_3, MgO, and $N_2C_3A_5$, respectively; I_α, I_i, I_{MgO}, and $I_{N_2C_3A_5}$ are the characteristic peak intensities of α-Al_2O_3, i phase, MgO, and $N_2C_3A_5$, respectively; RIR_α, RIR_i, RIR_{MgO}, and $\mathrm{RIR}_{N_2C_3A_5}$ are the reference intensity ratios of α-Al_2O_3, i phase, MgO, and $N_2C_3A_5$, respectively.

The Coats-Redfern method [21–24] was used to determine the reaction model, for which the Arrhenius equation is shown in Eq. (3). The value of $2RT/E$ is much smaller than 1, so $\ln\left[\frac{RA}{\beta E}\times\left(1-\frac{2RT}{E}\right)\right]$ can be regarded as a constant. Thus, the relation between $\ln\frac{G(\alpha)}{T^2}$ and $-\frac{E}{RT}$ is linear. Table 3 shows the kinetic models used for the solid-state reactions and the corresponding calculation results. The linear correlation coefficients R^2 of the A2, F1, and F2 models are greater than 0.99.

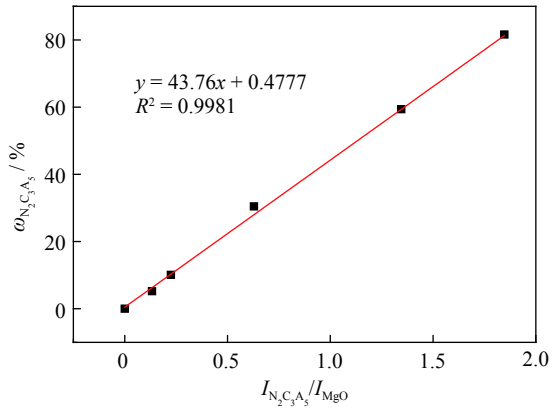

Fig. 14. Linear fit of $\omega_{N_2C_3A_5}$ and $I_{N_2C_3A_5}/I_{MgO}$.

$$\ln\frac{G(\alpha)}{T^2}=\ln\left[\frac{RA}{\beta E}\times\left(1-\frac{2RT}{E}\right)\right]-\frac{E}{RT} \quad (3)$$

where α is the formation percentage of $N_2C_3A_5$ (%), $G(\alpha)$ is the function related to α, T is the reaction temperature (K), A is the pre-exponential factor (s^{-1}), R is the gas constant ($J\cdot K^{-1}\cdot mol^{-1}$), β is the heating rate ($K\cdot min^{-1}$), and E is the activation energy ($kJ\cdot mol^{-1}$).

Table 4 shows the calculation results of the kinetic parameters A and E according to the A2, F1, and F2 models, respectively. The theoretical value of the pre-exponential factor should be between 10^6 and 10^{18} during the solid-state reaction process. Neither the A2 nor F1 model can explain the formation of $N_2C_3A_5$. Therefore, we considered the formation of $N_2C_3A_5$ to be the secondary reaction model of F2, which demonstrated that the formation process of $N_2C_3A_5$ was mainly controlled by the chemical reaction. The activation energy and the pre-exponential factor are 223.97 kJ/mol and 3.42×10^6 s^{-1}, respectively. The formation kinetics equation of $N_2C_3A_5$ is as follows:

$$(1-\alpha)^{-1}-1=3.42\times10^6\times e^{-\frac{223970}{RT}}\times t \quad (4)$$

Table 3. Solid-state reaction rate models and corresponding results

Item	Model	Symbol	$G(\alpha)$	Linear correlation (r)	R^2
Nuleation model	Power law	P2	$\alpha^{1/2}$	−0.9659	0.8993
	Power law	P3	$\alpha^{1/3}$	−0.9151	0.7561
	Power law	P4	$\alpha^{1/4}$	−0.6542	0.1419
	Avrami-Erofeev	A2	$[-\ln(1-\alpha)]^{1/2}$	−0.9970	0.9911
	Avrami-Erofeev	A3	$[-\ln(1-\alpha)]^{1/3}$	−0.9954	0.9861
	Avrami-Erofeev	A4	$[-\ln(1-\alpha)]^{1/4}$	−0.9919	0.9759
Diffusion model	1−D diffusion	D1	α^2	−0.9865	0.9598
	3−D diffusion Jander equation	D3	$[1-(1-\alpha)^{1/3}]^2$	−0.9964	0.9891
	3−D Ginstiing-Brounstein	D4	$1-2\alpha/3-(1-\alpha)^{2/3}$	−0.9939	0.9818
Reaction order and geometric contraction model	First order	F1	$-\ln(1-\alpha)$	−0.9980	0.9939
	Second order	F2	$(1-\alpha)^{-1}-1$	−0.9969	0.9907
	Contracting area (cylinder)	R2	$1-(1-\alpha)^{1/2}$	−0.9935	0.9805
	Contracting volume (sphere)	R3	$1-(1-\alpha)^{1/3}$	−0.9956	0.9867

Table 4. Calculation results for activation energy (E) and pre-exponential factor (A) of $N_2C_3A_5$

Symbol	E / ($kJ\cdot mol^{-1}$)	A / s^{-1}
A2	58.69	0.14
F1	139.11	500.56
F2	223.97	3.42×10^6

4. Conclusions

(1) The minerals formed during the sintering process in the $CaO-Al_2O_3-Na_2O$ system based on the chemical equivalent of $N_2C_3A_5$ mainly included $N_2C_3A_5$, CA, and $C_{12}A_7$. The $N_2C_3A_5$ content could reach about 92wt% when sintered at 1200°C for 30 min, the grains of which were much larger than those of $C_{12}A_7$ and CA.

(2) The formation of the $N_2C_3A_5$ crystal structure mainly occurred between 970 and 1100°C, and its intermediate phase $C_{12}A_7$ completely transformed into $N_2C_3A_5$ at a temperature less than 1100°C.

(3) The crystal system of $N_2C_3A_5$ was tetragonal, and the preferential crystal planes during growth were (110) and (210). The formation of $N_2C_3A_5$ followed a secondary reaction model, and the activation energy and pre-exponential factor were 223.97 kJ/mol and 3.42×10^6 s^{-1}, respectively.

Acknowledgements

This work was financially supported by the National Key R&D Program of China (No. 2018YFC1901903), the National Nature Science Foundation of China (Nos. 51674075 and 51774079), and the Fundamental Research Funds for the Central Universities, China (No. N182508026).

References

[1] N.K. Lee, K.T. Koh, S.H. Park, and G.S. Ryu, Microstructural

investigation of calcium aluminate cement-based ultra-high performance concrete (UHPC) exposed to high temperatures, *Cem. Concr. Res.*, 102(2017), p. 109.

[2] Y.Y. Zhang, W. Lü, Y.H. Qi, and Z.S. Zou, Recovery of iron and calcium aluminate slag from high-ferrous bauxite by high-temperature reduction and smelting process, *Int. J. Miner. Metall. Mater.*, 23(2016), No. 8, p. 881.

[3] R.M. Parreira, T.L. Andrade, A.P. Luz, V.C. Pandolfelli, and I.R. Oliveira, Calcium aluminate cement-based compositions for biomaterial applications, *Ceram. Int.*, 42(2016), No. 10, p. 11732.

[4] J.H. Chen, H.Y. Chen, M.W. Yan, Z. Cao, and W.J. Mi, Formation mechanism of calcium hexaluminate, *Int. J. Miner. Metall. Mater.*, 23(2016), No. 10, p. 1225.

[5] B. Hallstedl, Assessment of the $CaO-Al_2O_3$ system, *J. Am. Ceram. Soc.*, 73(1990), No. 1, p. 15.

[6] X.L. Pan, D. Zhang, Y. Wu, and H.Y. Yu, Synthesis and characterization of calcium aluminate compounds from gehlenite by high-temperature solid-state reaction, *Ceram. Int.*, 44(2018), No. 12, p. 13544.

[7] H. Verweij and C.M.P.M. Saris, Phase formation in the system $Na_2O{\cdot}Al_2O_3$–$CaO{\cdot}A1_2O_3$–Al_2O_3 at 1200 °C in air, *J. Am. Ceram. Soc.*, 69(1986), No. 2, p. 94.

[8] D. Zhang, W. Zhang, H.L. Sun, and B. Wang, Mineral transition mechanism of calcium aluminate with sodium doping during high-temperature sintering reaction, *J. Alloys Compd.*, 771(2019), p. 195.

[9] J. Yang, Q. Wang, J.Q. Zhang, O. Ostrovski, C. Zhang, and D.X. Cai, Effect of $Al_2O_3/(B_2O_3 + Na_2O)$ ratio on $CaO-Al_2O_3$-based mold fluxes: Melting property, viscosity, heat transfer, and structure, *Metall. Mater. Trans. B*, 50(2019), No. 6, p. 2794.

[10] J. Shen, L. Gong, and Q.X. Li, Structure and antibacterial property of Na_2O doped $C_{12}A_7$, *Chin. J. Inorg. Chem.*, 27(2011), No. 2, p. 353.

[11] C. Ostrowski and J. Żelazny, Solid solutions of calcium aluminates C_3A, $C_{12}A_7$ and CA with sodium oxide, *J. Therm. Anal. Calorim.*, 75(2004), No. 3, p. 867.

[12] H.Y. Yu, X.L. Pan, B. Wang, W. Zhang, H.L. Sun, and S.W. Bi, Effect of Na_2O on the formation of calcium aluminates in $CaO-Al_2O_3-SiO_2$ system, *Trans. Nonferrous Met. Soc. China*, 22(2012), No. 12, p. 3108.

[13] D. Zhang, X.L. Pan, H.Y. Yu, and Y.C. Zhai, Mineral transition of calcium aluminate clinker during high-temperature sintering with low-lime dosage, *J. Mater. Sci. Technol.*, 31(2015), No. 12, p. 1244.

[14] Y.P. Tian, X.L. Pan, H.Y. Yu, and G.F. Tu, Formation mechanism of calcium aluminate compounds based on high-temperature solid-state reaction, *J. Alloys Compd.*, 670(2016), p. 96.

[15] P. McMillan and B. Piriou, Raman spectroscopy of calcium aluminate glasses and crystals, *J. Non-Cryst. Solids*, 55(1983), No. 2, p. 221.

[16] K. Kajihara, S. Matsuishi, K. Hayashi, M. Hirano, and H. Hosono, Vibrational dynamics and oxygen diffusion in a nanoporous oxide ion conductor $12CaO{\cdot}7Al_2O_3$ studied by ^{18}O labeling and micro-Raman spectroscopy, *J. Phys. Chem. C*, 111(2007), No. 40, p. 14855.

[17] P. McMillan, B. Piriou, and A. Navrotsky, A Raman-spectroscopic study of glasses along the joins silica–calcium aluminate, silica–sodium aluminate, and silica–potassium aluminate, *Geochim. Cosmochim. Acta*, 46(1982), No. 11, p. 2021.

[18] A. Meiszterics, L. Rosta, H. Peterlik, J. Rohonczy, S. Kubuki, P. Henits, and K. Sinkó, Structural characterization of gel-derived calcium silicate systems, *J. Phys. Chem. A*, 114(2010), No. 38, p. 10403.

[19] L. Zhang, R. Lan, C.T.G. Petit, and S.W. Tao, Durability study of an intermediate temperature fuel cell based on an oxide–carbonate composite electrolyte, *Int. J. Hydrogen Energy*, 35(2010), No. 13, p. 6934.

[20] M.A. Legodi, D. de Waal, J.H. Potgieter, and S.S. Potgieter, Rapid determination of $CaCO_3$ in mixtures utilising FT-IR spectroscopy, *Miner. Eng.*, 14(2001), No. 9, p. 1107.

[21] S. Vyazovkin and C.A. Wight, Isothermal and non-isothermal kinetics of thermally stimulated reactions of solids, *Int. Rev. Phys. Chem.*, 17(1998), No. 3, p. 407.

[22] Š. Zuzjaková, P. Zeman, and Š. Kos, Non-isothermal kinetics of phase transformations in magnetron sputtered alumina films with metastable structure, *Thermochim. Acta*, 572(2013), p. 85.

[23] M.J. Cran, S.R. Gray, J. Scheirs, and S.W. Bigger, Non-isothermal depolymerisation kinetics of poly(ethylene oxide), *Polym. Degrad. Stab.*, 96(2011), No. 8, p. 1497.

[24] B.A. Sava, M. Elisa, C. Bartha, R. Iordanescu, I. Feraru, C. Plapcianu, and R. Patrascu, Non-isothermal free-models kinetic analysis on crystallization of europium-doped phosphate glasses, *Ceram. Int.*, 40(2014), No. 8, p. 12387.